ACS APPLIED MATERIALS & INTERFACES

Research Article

www.acsami.org

Enhanced Photocatalytic Degradation of Tetracycline by AgI/$BiVO_4$ Heterojunction under Visible-Light Irradiation: Mineralization Efficiency and Mechanism

Fei Chen,[†,‡] Qi Yang,[*,†,‡] Jian Sun,[†,‡] Fubing Yao,[†,‡] Shana Wang,[†,‡] Yali Wang,[†,‡] Xiaolin Wang,[†,‡] Xiaoming Li,[†,‡] Chenggang Niu,[†,‡] Dongbo Wang,[*,†,‡] and Guangming Zeng[†,‡]

[†]College of Environmental Science and Engineering, and [‡]Key Laboratory of Environmental Biology and Pollution Control, Ministry of Education, Hunan University, Changsha 410082, People's Republic of China

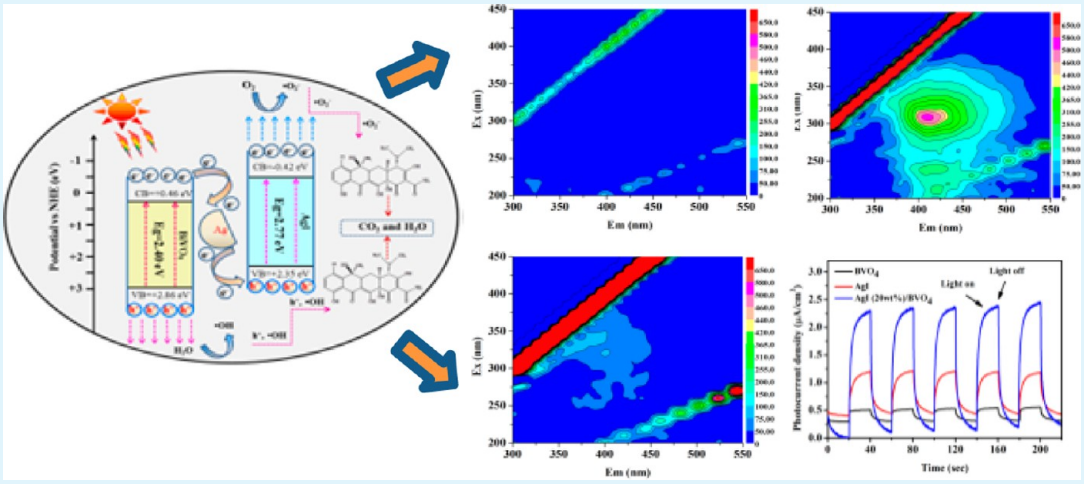

ABSTRACT: Recently, visible-light-driven photocatalysis is of great interest in the environmental pollutant remediation. In the present study, a novel heterostructured photocatalyst AgI/$BiVO_4$ was synthesized by an in situ precipitation procedure. The AgI/$BiVO_4$ heterojunctions exhibited excellent photoactivity for the refractory pollutant (tetracycline (TC), a typical antibiotic) decomposition under visible light illumination. The synthetic sample with 1:4 mass ratio of AgI:$BiVO_4$ possessed the highest photocatalytic performance in all of the as-prepared catalysts. The TC molecules were substantially eliminated (94.91%) within 60 min, and degradation efficiency was considerably better than those of bare $BiVO_4$ (62.68%) and AgI (75.43%) under identical conditions. Simultaneously, 90.46% of TOC removal was also achieved within 120 min, suggesting that the mineralization was superior and further confirmed by three-dimensional excitation−emission matrix fluorescence spectroscopy (3D EEMs). The XRD, XPS, DRS, and PL measurements revealed that a small amount of Ag nanoparticles was produced at the early photodegradation process. The structure transformation from AgI/$BiVO_4$ (double-type) to AgI/Ag/$BiVO_4$ (sandwich-like) improved the corresponding visible-light absorption performance. The self-assembly Z-scheme heterojunction that consisted of AgI, Ag, and $BiVO_4$ also efficiently accelerated photoinduced electron−hole pairs' separation and ultimately improved the efficiency of TC degradation. The responsible photocatalytic mechanism was discussed in detail on the basis of the reactive species capturing tests and ESR analysis, and the experimental results had been validated that superoxide radicals and holes played a vital role during the photocatalytic process. Furthermore, TC degradation efficiency was not of significant loss after four consecutive cycles, suggesting the excellent photostability of AgI/$BiVO_4$ nanocomposite. These features demonstrate that the AgI/$BiVO_4$ heterojunction has great application potential for refractory pollutants' removal from wastewater.

KEYWORDS: *photocatalysis, AgI/$BiVO_4$, tetracycline, mineralization, degradation mechanism*

1. INTRODUCTION

In the past few decades, the growing energy shortage crisis and environmental pollution have prompted considerable research in regard to solar energy utilization.[1−5] Semiconductor photocatalysis technique, as an economic and environment-friendly technology, has aroused widespread concern and been successfully employed to solve the above-mentioned problems.[6−8] Nevertheless, the photocatalytic performance of most semiconductor photocatalysts available located at a low level, and their practical applications were hampered by some internal defects, such as the poorer visible light utilization, the lower photogenerated electrons and holes pairs' separation, and the

Received: September 27, 2016
Accepted: November 16, 2016
Published: November 16, 2016

DOI: 10.1021/acsami.6b12278
ACS Appl. Mater. Interfaces 2016, 8, 32887−32900

lack of active species generation.[9−12] Thus, to maximize the exploration of solar light, the development of efficient and new-type visible light-driven (VLD) photocatalysis for industrial production is still an arduous task.

Very recently, ternary oxide semiconductor $BiVO_4$ (monoclinic scheelite) has become a promising photocatalyst because of its relatively narrow bandgap (about 2.40 eV), nontoxicity, chemical stability, and sunlight utilization for wastewater treatment.[13] Unfortunately, the photoinduced charge carriers of bare $BiVO_4$ tended to recombine promptly, resulting in an unsatisfying photocatalytic performance.[14,15] Up to now, the coupling of one semiconductor with the other one to construct heterostructured photocatalysts has been previously reported to greatly enhance the single semiconductor photoactivity, which was regarded as a feasible approach to solve the above-mentioned defects.[16] For example, Xu et al. reported that heterostructured sesame-biscuit-like $Bi_2O_2CO_3/Bi_2MoO_6$ nanoplates exhibited superior visible-light photoactivity for rhodamine B decomposition, and the corresponding degradation rate was about 64 times higher than that of pure Bi_2MoO_6.[17] Mu and his co-workers fabricated $In_2O_3-TiO_2$ heteroarchitectures via the electrospinning and solvothermal methods; the samples displayed substantially improved photocatalytic performance due to the better photogenerated electron−hole pairs' separation.[18] Certainly, intense efforts have been devoted to enhancing the photoactivity of pure $BiVO_4$ by constructing heterogeneous photocatalysts with other matched semiconductors, such as $BiVO_4/Ag_3VO_4$,[19] $BiVO_4/MoS_2$,[20] $Cu_2O/BiVO_4$,[21] $Bi_2S_3/BiVO_4$,[22] $BiVO_4/BiOI$,[23] and so on. For long-term photocatalysis development and deep photocatalytic mechanism insight, it is still necessary to seek out more suitable semiconductors, which could fabricate heterojunctions with $BiVO_4$.

By far, silver halide (AgCl, AgBr, and AgI)-based photocatalysts have been explored in the photocatalysis field, due to their perfect activities in the photo-oxidation of organic pollutants.[24,25] According to previous documents,[26,27] bare AgX is unstable and might be easily decomposed to Ag nanoparticles under visible light illumination, further to bring about the excess of metallic Ag on the surface of AgX along with the light irradiation time, resulting in a lower photocatalytic activity. In other words, its practical applications would be unavoidably hampered to some extent. The photostability and photoactivity of AgX-based nanocomposites could be improved by the deposition of AgX onto certain semiconductor materials.[28,29] For instance, Ye and his co-workers synthesized novel VLD $AgI/BiPO_4$ composite with both perferable visible light photocatalytic performance and good reusability.[30] Chen et al. found out Ag nanoparticles could be generated on an Ag_3PO_4/AgI composite surface during the early photocatalytic reaction, and the Z-scheme system promoted the photoinduced carriers separation and simultaneously enhanced the photostability.[31] Accordingly, the combination of AgI and $BiVO_4$ might seem to be reasonable. Meanwhile, much research had recommended that Ag compounds photocatalysts might follow a Z-scheme mechanism.[32,33] For example, He et al. had also designed $Ag_3PO_4/g\text{-}C_3N_4$ composite in converting CO_2 to fuels under simulated sunlight irradiation. A slight amount of Ag nanoparticles was generated under visible light illumination, and the Z-scheme system might form in the $Ag_3PO_4/g\text{-}C_3N_4$ hybrid. The formed Z-scheme system promoted an efficient photoinduced carriers separation and photocatalytic performance enhancement.[34]

Moreover, the conduction band of AgI (−0.42 eV) is more negative than that of $BiVO_4$ (+0.46 eV). On the contrary, the valence band of $BiVO_4$ (+2.86 eV) is more positive than that of AgI (+2.35 eV).[35,36] Thus, a typical charge separation and transportation might be built due to the similar heterojunction structure such as BiOBr/AgBr composite.[32] If slight metallic Ag produced in the $AgI/BiVO_4$ system, it might transfer to follow the Z-scheme mechanism described as before. The forming Ag would play an important role in accelerating the internal charge separation, and ultimately enhanced the photocatalytic activity. However, as far as we know, no corresponding research has been reported to discuss the new-type VLD $AgI/BiVO_4$ nanocomposite for refractory pollutants' removal from wastewater based on the Z-scheme mechanism.

Herein, novel $AgI/BiVO_4$ nanocomposite was commendably fabricated via the deposition-precipitation process. Antibiotic tetracycline (TC) was chosen as the target refractory pollutant. The AgI loading remarkably promoted the photocatalytic activity of $BiVO_4$ during the photo-oxidation process. The presence of Ag nanoparticles was validated by XRD, XPS, DRS, and PL analysis, which facilitated the generation of Z-scheme degradation mechanism. The origin of enhanced photoactivity for $AgI/BiVO_4$ composites was explored by thorough investigation of structure, morphology, and optical properties. The predominant radicals in the photodegradation system were discussed by radicals trapping experiment and ESR analysis.

2. EXPERIMENTAL SECTION

2.1. Synthesis of $BiVO_4$ and $AgI/BiVO_4$ Heterojunction. *2.1.1. Synthesis of Dumbbell-Shaped $BiVO_4$.* Dumbbell-shaped $BiVO_4$ was prepared through a facile water bath process. Briefly, while stirring, $Bi(NO_3)_3{\cdot}5H_2O$ (1.94 g, 4 mmol) was initially dispersed into a 50 mL mixed solution of C_2H_5OH:CH_3COOH:H_2O (10:10:30, volume ratio). Meanwhile, 4 mmol of NH_4VO_3 was also dispersed into a 20 mL ammonia solution ($v(NH_3{\cdot}H_2O)$:$v(H_2O)$ = 3:1). After two clear solutions were achieved, the latter was added dropwise into the former, followed by 30 min of stirring. The pH of the homogeneous dispersion was fitted to be 6.35 with concentrated $NH_3{\cdot}H_2O$. After a 3 h water bath (80 °C) reaction, the yellow precipitate was filtered, washed, and dumbbell-shaped $BiVO_4$ samples were obtained by 12 h of drying at 60 °C.

2.1.2. Synthesis of $AgI/BiVO_4$ Heterojunction. $AgI/BiVO_4$ heterojunction was fabricated by an in situ deposition-precipitation procedure. Typically, 1 mmol of $BiVO_4$ was dispersed in 50 mL of deionized water under ultrasonic processing. After that, 0.073, 0.153, 0.345, and 0.919 mmol of $AgNO_3$ were slowly added into the above suspension. After 30 min of stirring in the dark, a 25 mL solution containing 0.073, 0.153, 0.345, and 0.919 mmol of KI was slowly added into above suspension. The suspension was stirred for another 3 h to synthesize the samples with the theoretical mass ratios of AgI to ($AgI+BiVO_4$) of 5, 10, 20, and 40 wt %, respectively. The samples were obtained by filtration, rinsed, and dried at 60 °C for the whole night. For comparison, bare AgI nanoparticles were also fabricated under conditions identical to those of $AgI/BiVO_4$ in the absence of $BiVO_4$.

2.2. Characterization. The structure and crystallinity were analyzed by powder X-ray diffraction (XRD) measurements on a D/max 2500v/pc X-ray diffractometer. Field emission scanning electron microscopy (FESEM, Hitachi S-4800) was employed to investigate the morphologies. The microstructures were also tested by transmission electron microscopy (TEM, FEI Tecnai G20). X-ray photoelectron spectroscopy (XPS) was conducted on a Thermo ESCALAB 250XI spectrometer. UV−vis adsorption spectroscopy (UV−vis DRS) was tested with a UV−vis spectrometer (UV-4100). The mineralization ability was verified by total organic carbon (TOC) measurements. Three-dimensional excitation−emission matrix fluorescence spectra (3D EEMs) were examined by a F-4500 spectrofluorimeter, and the

DOI: 10.1021/acsami.6b12278
ACS Appl. Mater. Interfaces 2016, 8, 32887−32900

excitation (λ_{ex}) or emission wavelengths (λ_{em}) were 200−450 or 300−550 nm, respectively. Photoluminescence (PL) spectra were carried out on an Edinburgh FLsp920 transient fluorescence spectrometer. The electron spin resonance (ESR) measurements were obtained on a Bruker ER200-SRC spectrometer (visible light, λ > 420 nm). Photocurrent (PT) and electrochemical impedance spectroscopy (EIS) were performed on an electrochemical workstation (CHI660C) in a typical three-electrode system.

2.3. Photoreaction Procedures. TC, a typical antibiotic, was used to evaluate the photocatalytic activities. A 300 W Xe lamp (λ > 420 nm) was used in the whole photodegradation reaction. Briefly, 0.03 g of catalyst was suspended into TC solution (100 mL, 20 mg/L). Before illumination, the suspension was constantly stirred for 30 min under the darkness to reach the absorption−desorption equilibrium. During visible light exposure, 4 mL aliquots were collected at a given interval and centrifuged. The filtrates were analyzed at the absorption wavelength of 357 nm by a UV−vis spectrophotometer (UV-4100). The degradation efficiency could be calculated as follows (eq 1):

$$\text{degradation efficiency (\%)} = \left(1 - \frac{C_t}{C_0}\right) \times 100\% = \left(1 - \frac{A_t}{A_0}\right) \times 100\% \quad (1)$$

where C_0 and C_t represent the concentrations of TC at irradiation time 0 and t, respectively. A_t and A_0 are the corresponding values for TC absorbance.

3. RESULTS AND DISCUSSION

3.1. Materials' Characterization. The crystalline nature and composition of pure $BiVO_4$, pure AgI, and AgI/$BiVO_4$ nanocomposites were first characterized by XRD technology. As depicted in Figure 1, the peaks of $BiVO_4$ at 2θ values of

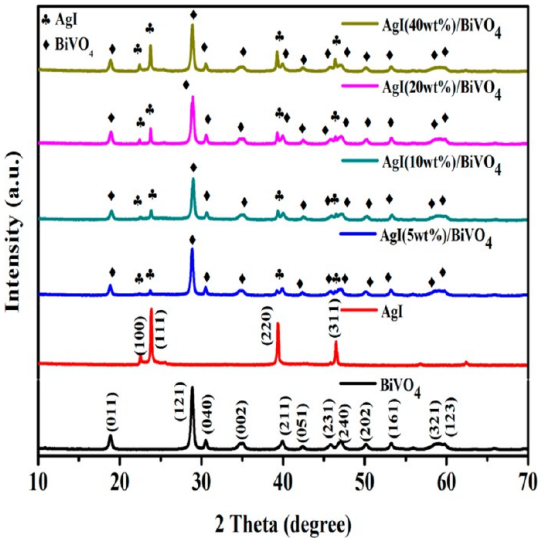

Figure 1. XRD patterns of pure $BiVO_4$, pure AgI, and AgI/$BiVO_4$ with different weight ratios.

18.63°, 28.82°, 30.56°, 35.20°, 39.75°, 42.44°, 45.43°, 46.72°, 49.95°, 53.33°, 55.28°, and 59.27° could be ascribed to (011), (121), (040), (002), (211), (051), (231), (240), (202), (161), (321), and (123) crystal planes of $BiVO_4$ (JCPDS file no. 14-0688),[19] respectively. The characteristic peaks of AgI were ascribed to hexagonal β-AgI (JCPDS file no. 09-0374).[28] In the XRD patterns of AgI/$BiVO_4$ nanocomposites, a good coexistence of two phases (AgI and $BiVO_4$) was perceived, indicating AgI was successfully introduced into the $BiVO_4$ systems. In addition, the AgI diffraction peaks intensities increased with the weight ratios, and the result was consistent with the increasing AgI amounts in the preparation. All of the catalysts showed the same diffraction peaks of AgI and $BiVO_4$, suggesting that AgI loading did not significantly change on the $BiVO_4$ phase.

XPS test results of Ag 3d, I 3d, Bi 4f, and V 2p for AgI(20 wt %)/$BiVO_4$ were presented in Figure 2. The survey XPS spectrum of AgI(20 wt %)/$BiVO_4$ (Figure 2A) displayed that the predominant elements of the samples were C, Bi, V, O, Ag, and I. The presence of C (284.6 eV) might be the fact that the XPS instrument itself possessed the adventitious hydrocarbon.[37] Two peaks at 367.4 and 373.6 eV belonged to Ag $3d_{5/2}$ and Ag $3d_{3/2}$, respectively (Figure 2B).[19] The two peaks could not been divided into four peaks, indicating only the existence of Ag^+ among AgI/$BiVO_4$ composites. The peaks at 619.4 and 630.9 eV in high-resolution I 3d spectra (Figure 2C) were attributed to I $3d_{5/2}$ and I $3d_{3/2}$, respectively.[28] Figure 2D showed the high-resolution Bi 4f spectra; two typical peaks appearing at 159.4 and 164.8 eV were assigned to Bi $4f_{7/2}$ and Bi $4f_{5/2}$, respectively.[23] Two obvious peaks situated at banding energies of 517.1 and 524.2 eV were clearly perceived in Figure 2E, which should belong to V $2p_{3/2}$ and V $2p_{1/2}$, respectively.[38] The high-resolution XPS spectrum of O 1s was observed in Figure 2F, and the characteristic peak was detected to be 530.7 eV. The XPS results further confirmed the successful combination of $BiVO_4$ and AgI.

The morphological evolution of various catalysts was examined by SEM analysis (Figure 3A−F). From Figure 3A, pure $BiVO_4$ had a unique dumbbell-shaped morphology, smooth surface, and uniform distribution. As displayed in Figure 3B, AgI samples were mainly composed of irregular nanoparticles with diameters of 10−150 nm. Both types of morphologies were found in AgI(20 wt %)/$BiVO_4$ nanocomposite (Figure 3C,D). The detailed structural information was also detected by TEM technology. For $BiVO_4$ (Figure 3E), regular and smooth dumbbell-shaped morphologies were presented. According to the TEM images of AgI(20 wt %)/$BiVO_4$ (Figure 3F), it was revealed that a certain amount of irregular nanoparticles distributed on the surface (rough) and vicinity of dumbbell-shaped $BiVO_4$, indicating that AgI and $BiVO_4$ were well combined with each other. In addition, the HRTEM image of AgI(20 wt %)/$BiVO_4$ was also provided (Figure 3G). Two obvious lattice spacings of 0.231 and 0.308 nm coincided with the values for the (220) and (121) planes of AgI and $BiVO_4$, respectively. These results were the proofs for the formations of AgI/$BiVO_4$ heterojunctions.

3.2. Evaluation of Photocatalytic Activity. Tetracycline (TC), as a typical antibiotic, was selected as the model pollutant to evaluate the photoactivity of catalyst. As presented in Figure 4A, single $BiVO_4$ displayed poor photocatalytic activity with only 62.68% of TC degradation after 1 h irradiation. Simultaneously, for pure AgI, it could decompose about 75.43% of TC degradation. As compared to $BiVO_4$ and AgI, AgI/$BiVO_4$ samples showed more superior photocatalytic performance. With the increasing AgI amount in the nanocomposite, the photoactivity of AgI/$BiVO_4$ raised initially, and then when the ratio of AgI was beyond 20 wt %, the degradation efficiency of TC began falling. The AgI(20 wt %)/$BiVO_4$ exhibited the highest degradation efficiency (94.91%) within 1 h of visible-light irradiation. The better photocatalytic performance of deduced AgI-modified $BiVO_4$ should be attributed to the forming heterojunction and efficient

DOI: 10.1021/acsami.6b12278
ACS Appl. Mater. Interfaces 2016, 8, 32887−32900

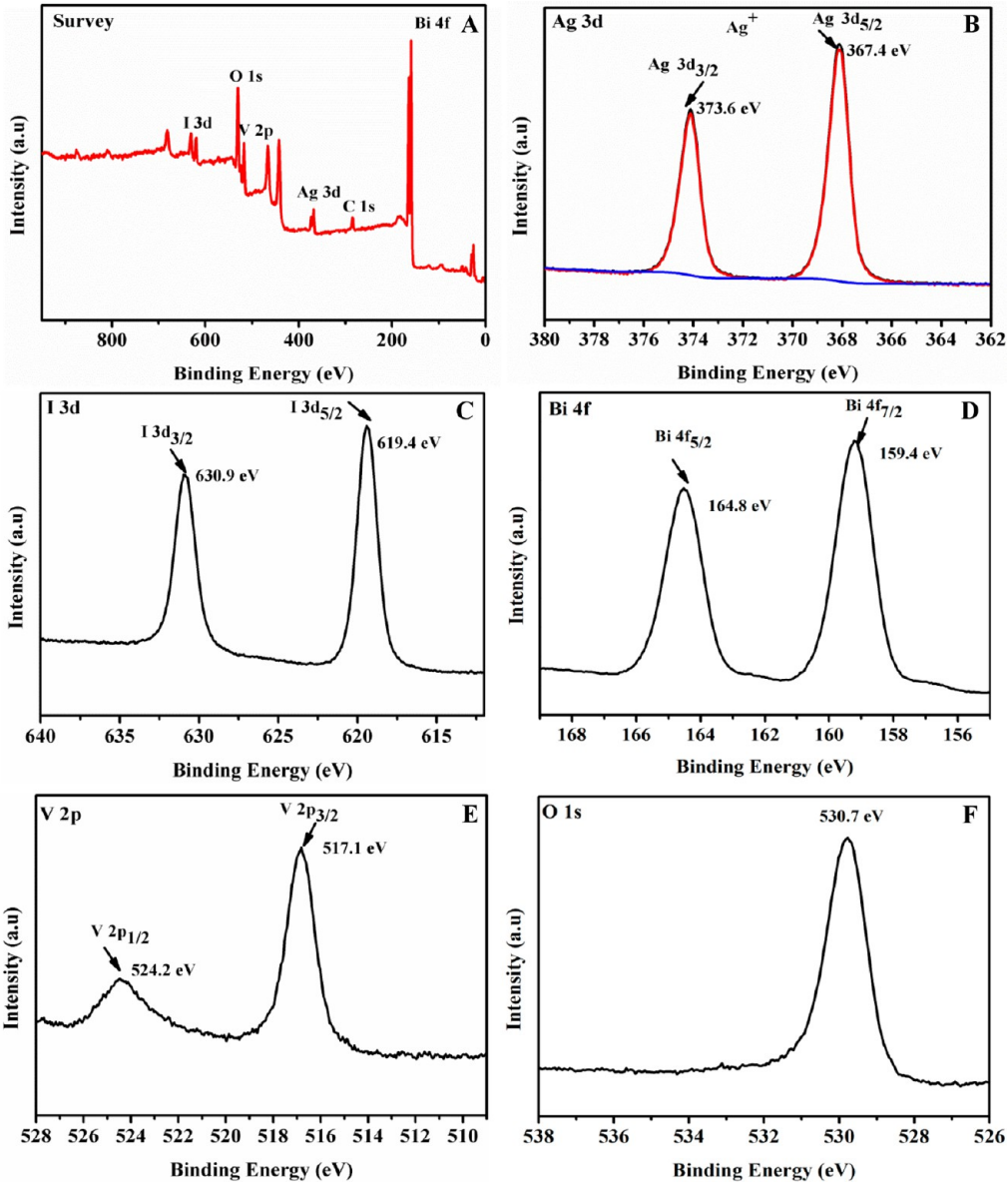

Figure 2. XPS spectra of AgI(20 wt %)/$BiVO_4$ sample: (A) survey scan and (B) Ag 3d, (C) I 3d, (D) Bi 4f, (E) V 2p, and (F) O 1s.

photoinduced electron−holes pairs' separation in the reaction system.

To give a deep insight of the photocatalytic oxidation process, the experimental results were simulated by pseudo-first-order kinetic model, and the results were listed in Figure 4B and Table 1. The photocatalytic process fitted well with a pseudo-first-order model ($R^2 > 0.98$), expressed as follows (eq 2):[35]

$$\ln\left(\frac{C_t}{C_0}\right) = -k_{app}t \quad (2)$$

where k_{app} is the apparent rate constant (min^{-1}). C_0 and C_t are the TC concentrations at reaction time 0 and t, respectively.

The k_{app} values for TC degradation with $BiVO_4$ and AgI were 0.0182 and 0.0304 min^{-1}, respectively. For AgI-modified $BiVO_4$, heterojunctions with AgI contents of 5, 10, 20, and 40 wt % exhibited much stronger photocatalytic performance, and the decomposition rate constants were calculated to be 0.0355, 0.0424, 0.0527, and 0.0401 min^{-1}, respectively. The k_{app} of the AgI (20 wt %)/$BiVO_4$ sample was the biggest, which was up to 2.89-fold higher than that of $BiVO_4$ and 1.74-fold higher than AgI. The results demonstrated that the introduction of AgI in AgI/$BiVO_4$ nanocomposites accelerated the photocatalytic degradation rate, attributable to the construction of hetero-junction structure between AgI and $BiVO_4$. Furthermore, the suitable amount of AgI would make a better synergistic effect, and the optimal AgI weight ratio was verified to be 20 wt %, which was consistent with the previously described photo-degradation results.

Indeed, TC concentration may vary tremendously in real applications. As shown in Figure 4C, a series of higher initial TC concentrations were set at 20, 30, 40, 50, and 60 mg/L, respectively. Along with the increasing TC concentrations, the decomposition efficiencies decreased to a certain extent, from 94.91% (20 mg/L) to 58.86% (60 mg/L). The reduction reason might be concluded from the following aspects: (1) Higher initial TC concentrations would result in the increase of the pathway length of photons entering the reaction system and the descending photons on the surface of the catalyst. (2)

DOI: 10.1021/acsami.6b12278
ACS Appl. Mater. Interfaces 2016, 8, 32887−32900

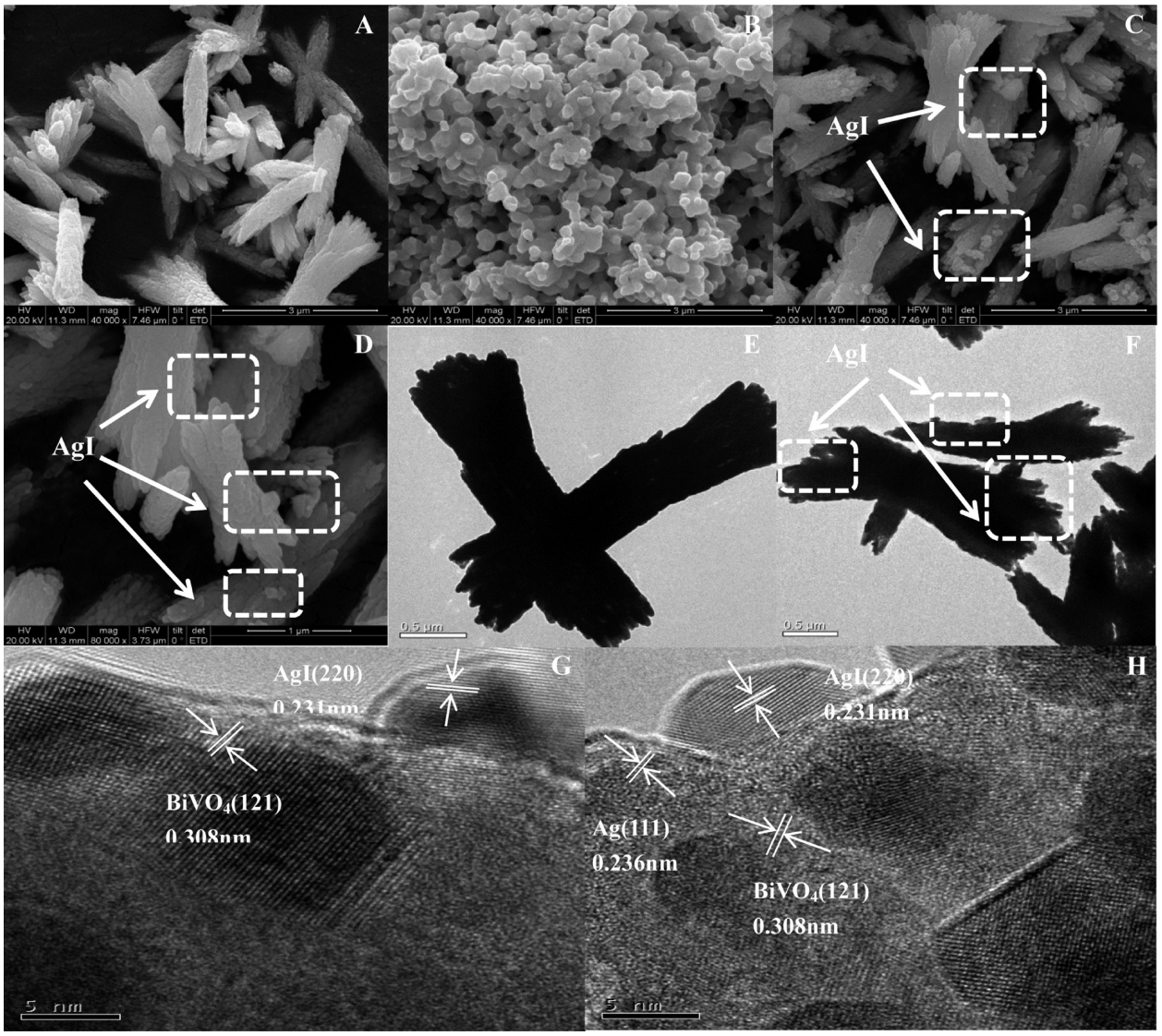

Figure 3. SEM images of the as-prepared samples: (A) pure $BiVO_4$, (B) pure AgI, and (C,D) AgI(20 wt %)/$BiVO_4$; typical TEM images of pure $BiVO_4$ (E), AgI(20 wt %)/$BiVO_4$ (F), and HRTEM images of the fresh (G) and the used (H) AgI(20 wt %)/$BiVO_4$.

There is an enhanced adsorption competition between TC and TC degradation products (intermediates) on catalyst surface, because more intermediates would be produced at higher pollutant concentration.[15,28] Although TC concentration could not been set at a detailed value, lower TC concentration was more beneficial to achieve higher TC removal in practical wastewater treatment. For example, the wastewater containing high concentration TC should be pretreated by dilution, cyclic treatment, and even the advanced oxidation process.

Moreover, salts with a different concentration involved in practical wastewater might pose a significant impact on TC removal. As a result, the effects of ion strength (NaCl, chosen as a reference) were taken into discussion. Detecting from Figure 4D, TC degradation efficiencies significantly decreased as the NaCl concentration increased from 0 to 0.1 mol/L but showed less reduction in the range of 0.1−0.5 mol/L. Two major reasons could explain the above-mentioned phenomenon. For one, the electrostatic protection would be emerged with the addition of NaCl, and the immediate electrostatic interaction between TC molecules and the catalyst was hampered. For the other, there was a competitive adsorption between TC and Na^+ ions on the reaction region, and this competition enhanced with NaCl amounts.[39] Thus, moderate pretreatment (such as dilution) of TC-containing wastewater with high salts level is necessary. The above parameter discussions were obtained over AgI (20 wt %)/$BiVO_4$ photocatalysis.

3.3. Mineralization Ability of AgI/$BiVO_4$ for TC and 3D EEMs Analysis. The mineralization ability is also an essential parameter to evaluate the photocatalytic properties of semiconductor photocatalysts. Figure 5 depicted the TC degradation in terms of total organic carbon (TOC) removal by different catalysts. The decomposition efficiencies reached about 8.98%, 21.81%, and 56.28% for pure $BiVO_4$, pure AgI, and AgI(20 wt %)/$BiVO_4$, respectively, within the irradiation time of 60 min. The obtained information indicated that AgI(20 wt %)/$BiVO_4$ nanocomposite could effectively mineralize TC into small intermediates or directly CO_2 and H_2O. When the illumination time was lengthened to 120 min, the TOC removal over the AgI(20 wt %)/$BiVO_4$ sample increased to 90.46% (Table 2), validating a promising application potential for wastewater treatment.

DOI: 10.1021/acsami.6b12278
ACS Appl. Mater. Interfaces 2016, 8, 32887−32900

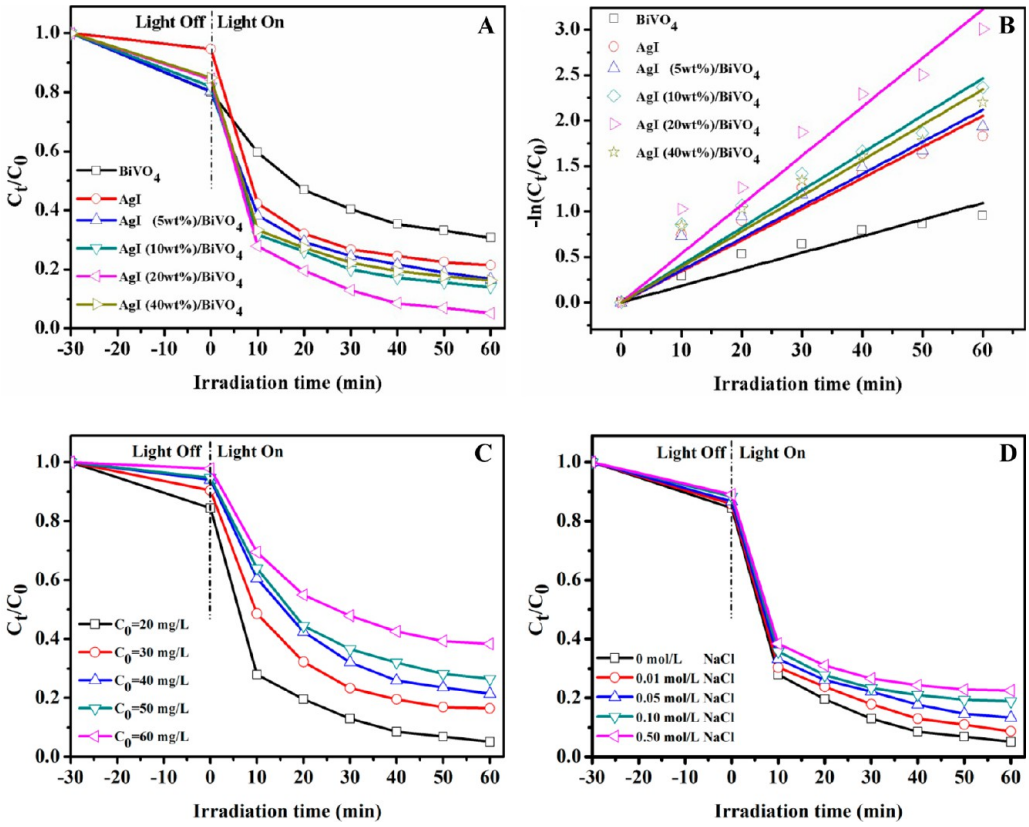

Figure 4. (A) Photocatalytic degradation of TC over AgI/$BiVO_4$ samples, (B) pseudo-first-order kinetics of TC degradation, (C) effect of initial TC concentration, and (D) effect of NaCl concentration.

Table 1. Pseudo-First-Order Rate Constants (k_{app}), Correlation Coefficients (R^2), and Degradation Efficiencies for the TC in Different Photocatalytic Systems

	TC (ln $C_t = -k_{app}t$ + ln C_0, pseudo-first-order reaction)			
catalyst	k_{app} (min^{-1})	R^2	standard error[a]	DE (%)
$BiVO_4$	0.0182	0.9862	0.0012	62.68 ± 2.33
AgI	0.0304	0.9825	0.0024	75.43 ± 2.07
AgI(5 wt %)/$BiVO_4$	0.0355	0.9901	0.0022	80.12 ± 2.89
AgI(10 wt %)/$BiVO_4$	0.0424	0.9908	0.0025	85.39 ± 1.46
AgI(20 wt %)/$BiVO_4$	0.0547	0.9807	0.0028	94.91 ± 1.56
AgI(40 wt %)/$BiVO_4$	0.0401	0.9844	0.0025	84.41 ± 3.09

[a](I) The standard error referred to that of the slope in the equations. (II) Experimental conditions: 30 mg of catalyst, 100 mL of 20.0 mg/L TC aqueous solution, visible light (λ > 420 nm, 300 W Xe lamp).

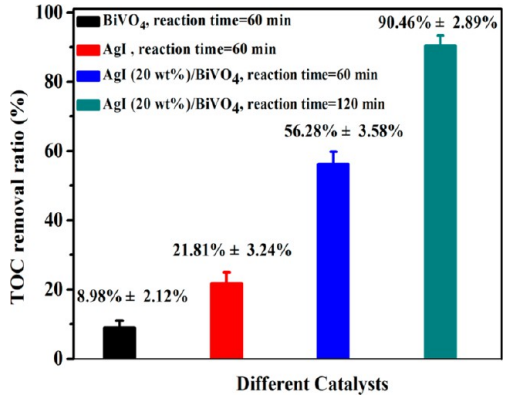

Figure 5. TOC removal by pure $BiVO_4$, AgI, and AgI(20 wt %)/$BiVO_4$.

For a more in-depth investigation of the photocatalytic degradation and mineralization property, 3D EEMs technology was also adopted. As shown in Figure 6, samples mappings were collected in both adsorption and photodecomposition process. EEMs were obtained under the following conditions: Figure 6A, taken from original sample; Figure 6B, collected after 30 min adsorption in darkness; and Figure 6C–F, an irradiation time of 10, 30, 60, and 120 min, respectively. According to previous reports, 3D EEMs had demonstrated the fact that the fluorescence quenching effect existed in the emergence of TC.[40,41] Wang and his co-workers[39] had also reported that two predominant peaks (peak A at $\lambda_{ex}/\lambda_{em}$ = (305–330 nm)/(430–450 nm) and peak B at $\lambda_{ex}/\lambda_{em}$ = (240–250 nm)/(435–450 nm)) could be discovered when TC molecules began to decompose. The two peaks could be attributable to the humic acids-like and fulvic acids-like fluorescence region, respectively. As revealed in Figure 6A,B, no signals were observed, indicating that TC molecules were not decomposed into other products during the adsorption procedure. When the samples were collected from the irradiation times of 10 min (Figure 6C), 30 min (Figure 6D), and 60 min (Figure 6E), the fluorescence signals increased with the reaction time (under visible light). The detailed fluorescence spectra parameters were listed in Table 2. Extending the irradiation time to 120 min (Figure 6F), the fluorescence intensity decreased from 530.45 to 35.29, suggesting the humic acids-like matter and fulvic acids-like matter had been degraded, which might be mineralized to other

DOI: 10.1021/acsami.6b12278
ACS Appl. Mater. Interfaces 2016, 8, 32887–32900

Table 2. TOC Removal by AgI(20 wt %)/$BiVO_4$ and Fluorescence Spectra Parameters along with the Irradiation Time *n*

reaction time (min)	TOC removal ratio (%)	fluorescence spectra parameters		
		peak A[a,b]	peak B[a,b]	intensity
stock solution	0			
dark (30)	0			
light (10)	17.13	310/420		8.32
light (30)	36.19	310/425	240/425	352.76
light (60)	56.28	310/410	240/420	530.45
light (120)	90.46	320/420		35.29

[a,b](I) (a) and (b) represented the two maxima peaks ascribed to the humic acids-like and fulvic acids-like fluorescence region, respectively. (II) Experimental conditions: 30 mg of catalyst, 100 mL of 20.0 mg/L TC aqueous solution, visible light (λ > 420 nm, 300 W Xe lamp).

intermediates or directly decomposed into CO_2 and H_2O. The result was in good accordance with the 90.46% of TOC removal within the same irradiation time, demonstrating that AgI(20 wt %)/$BiVO_4$ exhibited superior mineralization ability toward TC degradation.

3.4. Light Absorption, Photoluminescence, and Photoelectrochemical Properties. The optical property could be employed as a reference to evaluate the light absorption region. The light absorption properties of the as-synthesized samples were characterized by UV−vis DRS and presented in Figure 7A. Pure $BiVO_4$ and pure AgI have an absorption threshold at approximately 517 and 447 nm, respectively, which fitted well with the previous reports.[20,31] Unlike the above two single-component photocatalysts, AgI(20 wt %)/$BiVO_4$ presented a wider photoabsorption in the range of 250−800 nm. The cocatalytic effect between AgI and $BiVO_4$ should be responsible for the light absorption enhancement. The bandgap edge (E_g) of a semiconductor can evaluate the electron−hole pairs production and transformation. The relationship of band edge and optical absorption could be descried by the following formula (eq 3):[16]

$$\alpha h\nu = A(h\nu - E_g)^{n/2} \quad (3)$$

where A, E_g, h, α, and ν are proportionality constant, band gap, Planck constant, absorption coefficient, and light frequency, respectively. The absorption coefficient α was calculated from k (extinction coefficient) using $\alpha = 4\pi k/\lambda$. The changes of $(\alpha h\nu)^2$ as a function of the energy of incident photons ($h\nu$) were depicted in Figure 7A, and the E_g values of $BiVO_4$ and AgI were approximately 2.40 and 2.77 eV, respectively.

Photoluminescence (PL) spectroscopy has been widely employed to study the photogenerated charge carriers excitation and transfer in photocatalysis over semiconductors. Generally speaking, lower PL signals suggest the higher photoinduced electron−hole pairs' separation efficiency.[42] Figure 7B presented the PL spectra of $BiVO_4$ and AgI(20 wt %)/$BiVO_4$ with the excitation wavelength of 425 nm. Pure $BiVO_4$ displayed the higher PL intensity. In contrast, AgI(20 wt %)/$BiVO_4$ nanocomposite possessed the lower PL signal. The result indicated that the recombination rate of photoinduced electrons and holes pairs was efficiently inhibited through the combination of $BiVO_4$ and AgI.

Photocurrent tests (PT) were also performed to detect the photoresponses of pure $BiVO_4$, pure AgI, and AgI(20 wt %)/$BiVO_4$ nanocomposite. Maintaining identical operational

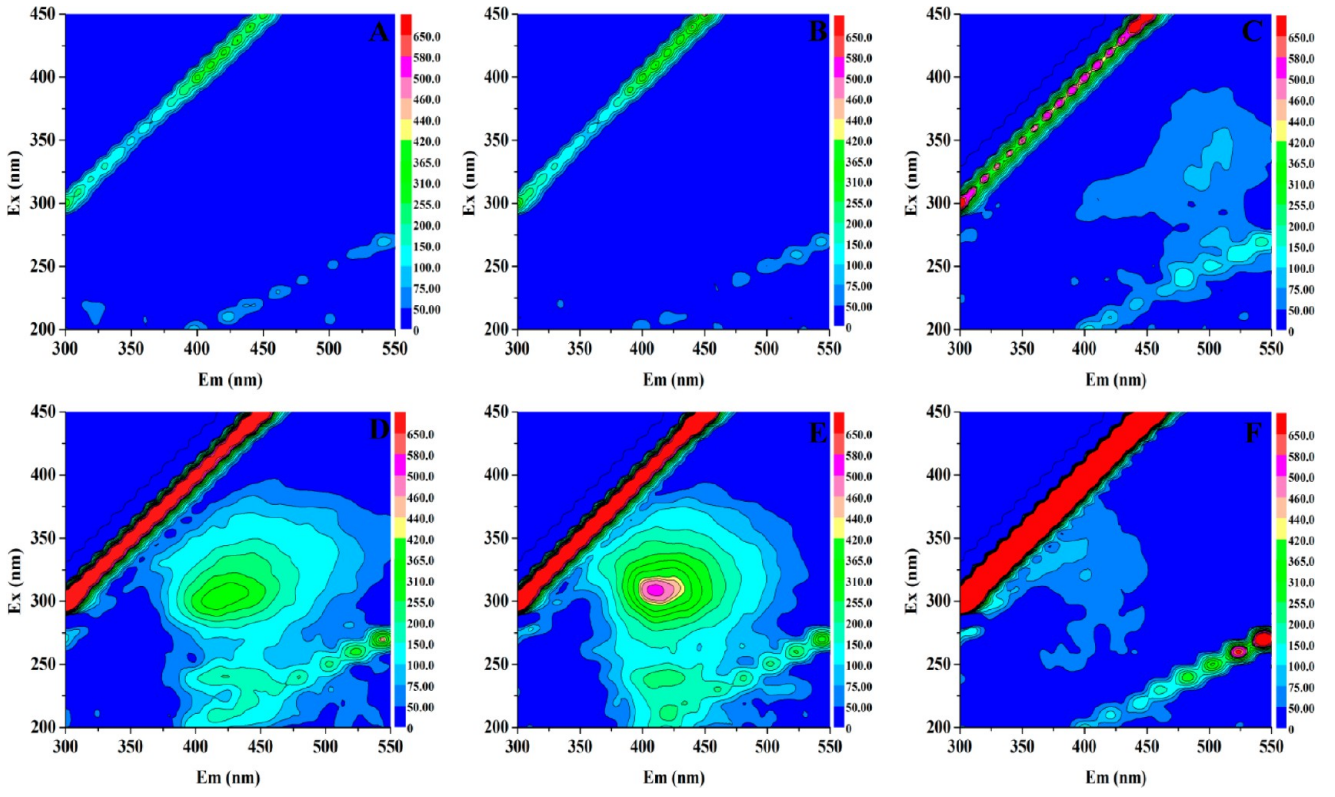

Figure 6. 3D EEMs of the aqueous solution: (A) taken from the original solution; (B) collected after 30 min adsorption in dark; and (C−F) obtained after an irradiation time of 10, 30, 60, and 120 min, respectively.

DOI: 10.1021/acsami.6b12278
ACS Appl. Mater. Interfaces 2016, 8, 32887−32900

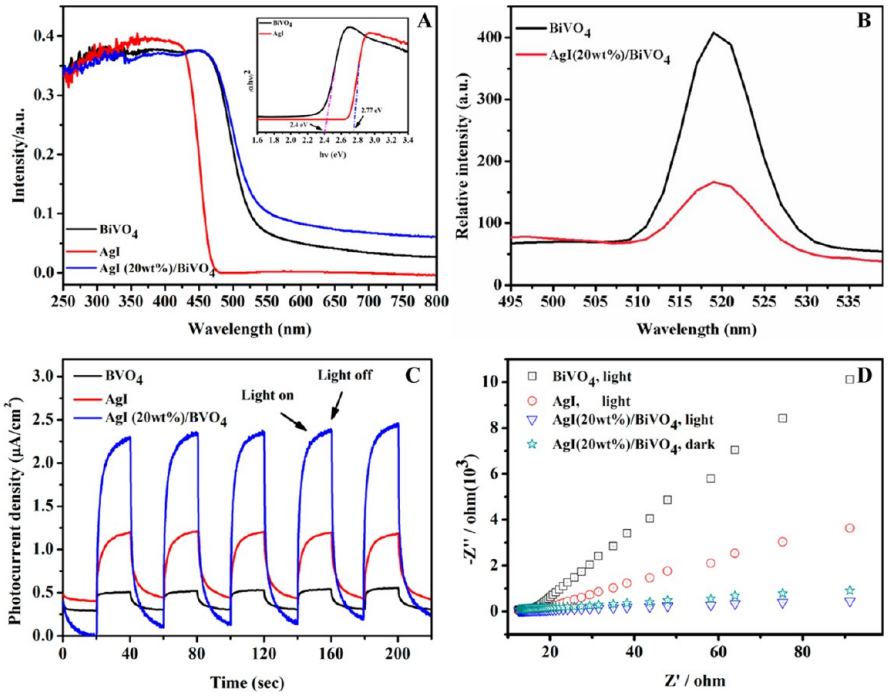

Figure 7. (A) UV−vis reflectance spectra of $BiVO_4$, AgI, and AgI(20 wt %)/$BiVO_4$; (B) PL spectra of $BiVO_4$, AgI, and AgI(20 wt %)/$BiVO_4$ samples with the excitation wavelength of 400 nm; (C) photocurrent responses of $BiVO_4$, AgI, and AgI(20 wt %)/$BiVO_4$ samples; and (D) EIS spectra of $BiVO_4$, AgI, and AgI(20 wt %)/$BiVO_4$.

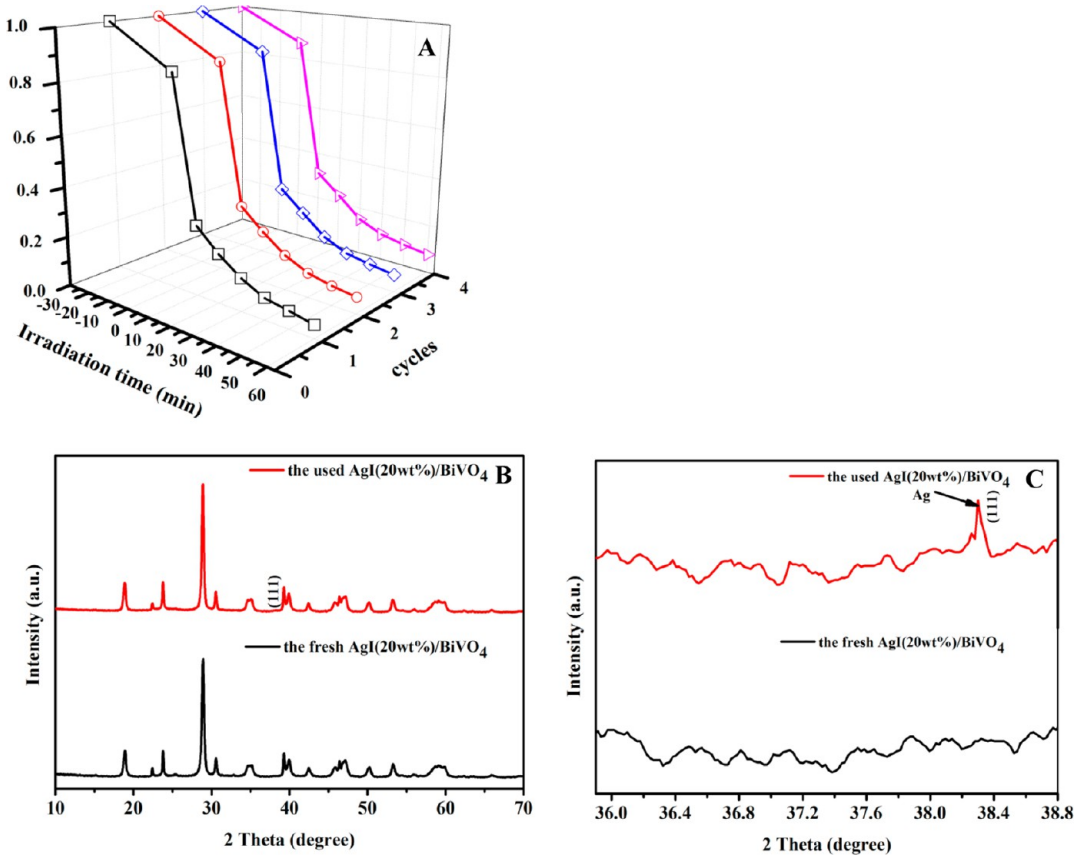

Figure 8. (A) Cycling test for the photocatalytic degradation of TC (20 mg/L) by AgI(20 wt %)/$BiVO_4$ and (B,C) XRD patterns of the fresh and used AgI(20 wt %)/$BiVO_4$.

conditions, the higher photocurrent intensity implies more efficient electron−hole pairs' separation.[38] As displayed in Figure 7C, although all three samples exhibited a quick response when the as-prepared working electrode was exposed

DOI: 10.1021/acsami.6b12278
ACS Appl. Mater. Interfaces 2016, 8, 32887−32900

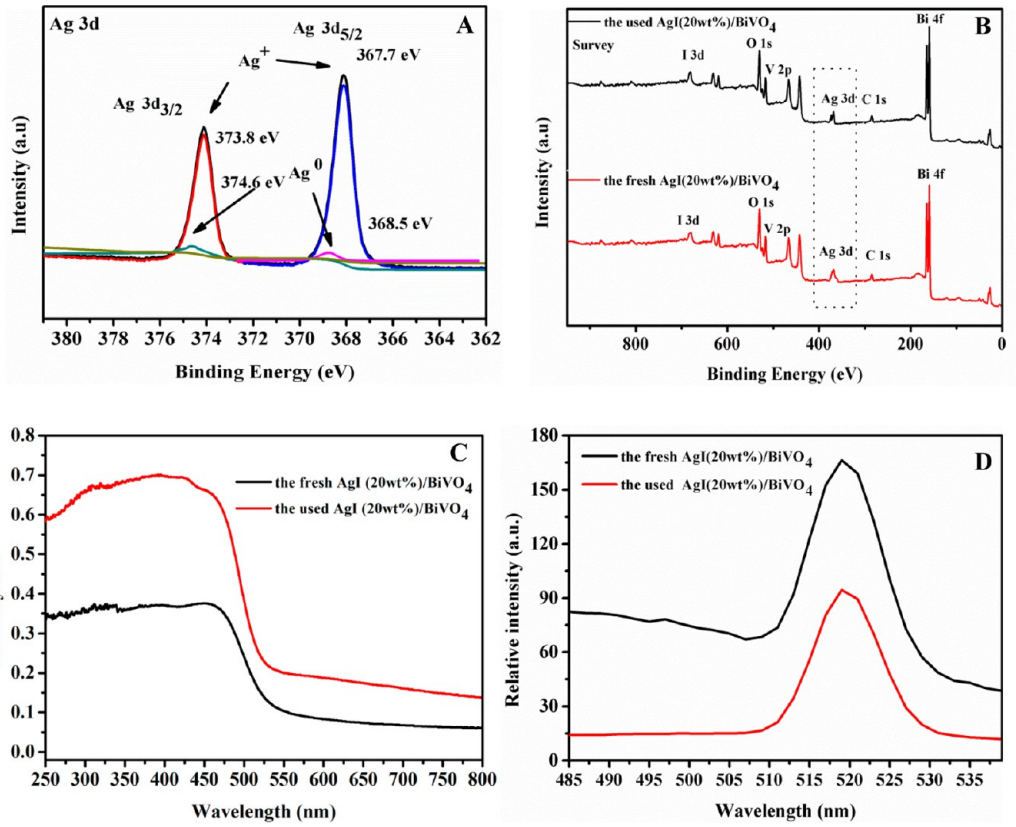

Figure 9. Comparison of the Ag 3d XPS spectra (A), the survey XPS spectra (B), DRS (C), and PL spectra (D) for the used and fresh AgI(20 wt %)/$BiVO_4$ nanocomposite.

to the light, the generated transient photocurrent was different. Under visible light irradiation, the photocurrent density collected by AgI(20 wt %)/$BiVO_4$ electrode was 2.15 ± 0.06 mA cm^{-2}, which was much higher than those of AgI and $BiVO_4$. The information inferred that the coeffects of AgI and $BiVO_4$ in the heterojunction could lead to produce more charge carriers and to favorably separate electrons.

The arc radius of the EIS Nyquist could be used as an effective method to reflect the charge transfer rate.[43,44] Generally, a smaller arc in the EIS Nyquist plot indicated a smaller charge-transfer resistance. As depicted in Figure 7D, the relative arc sizes for the as-prepared electrodes were presented in the following order: AgI(20 wt %)/$BiVO_4$ (light) < AgI(20 wt %)/$BiVO_4$(darkness) < AgI(light) ≪ $BiVO_4$(light), suggesting that the photoexcited charge carriers had generated and AgI(20 wt %)/$BiVO_4$ nanocomposite possessed the lowest resistance. The unique property made the AgI(20 wt %)/$BiVO_4$ nanocomposite present as the highest electron−hole pairs' separation and electron transfer efficiency, and the faster interfacial charge transfer to electron donor/acceptor, which agreed well with the results of PL and PT tests.

3.5. Photostability of AgI(20 wt %)/$BiVO_4$ Nanocomposite. The photostability investigation of AgI(20 wt %)/$BiVO_4$ was displayed in Figure 8A. After each run, the catalyst was collected, washed with deionized water to remove the residual TC, and then put into the fresh TC solution to begin new cycle. During the recycling experiments, all experimental conditions were kept exactly the same with first cycle experiment. No visible reduction in the decomposition efficiency of TC was found, and the removal rate could still reach 91.46% in the fourth run (while it was 94.91% for the first run). This result demonstrated that AgI(20 wt %)/$BiVO_4$ was a stable VLD photocatalyst for photocatalytic oxidation of refractory pollutants. Moreover, the used AgI(20 wt %)/$BiVO_4$ nanocomposite was characterized by XRD and XPS. Taking the fresh sample into comparison (Figure 8B), there was little discrepancy in the XRD patterns before and after the photocatalytic reaction. Only a weak peak at 38.38° could be ascribed to the (111) crystal planes of metallic Ag (JCPDS card no. 65-2871),[24] suggesting the low Ag content. To confirm this point, the partial XRD patterns were taken out and amplified, as revealed in Figure 8C. The peak at 38.38° was clearly perceived in the used sample, suggesting metallic Ag generated in the photodegradation procedure. At the same time, the HRTEM image of the used AgI(20 wt %)/$BiVO_4$ was also presented in Figure 3H. The *d*-spacing estimated to be 0.236 nm was fitted well with the (111) lattice plane of metallic Ag (JCPDS card no. 65-2871). As shown in Figure 9A, the Ag $3d_{5/2}$ and Ag $3d_{3/2}$ peaks could be divided into four characteristic peaks, where 374.6 and 373.8 eV belonged to Ag $3d_{3/2}$ and the other two peaks (368.5 and 367.7 eV) were for Ag $3d_{5/2}$, respectively. The two new peaks situated at 374.6 and 368.5 eV were assigned to elemental Ag.[27,31] In the survey XPS spectrum of the used sample (Figure 9B), the molar ratio of Ag/I was estimated to be 1.09:1, and it was higher than the theoretical ratio (1:1) for the fresh AgI(20 wt %)/$BiVO_4$. That was to say, metallic Ag was formed in the photocatalytic reaction and was favorable to the light absorption due to its SPR effect and the photoinduced electron−hole pairs' separation enhancement.

To further confirm the above speculation, DRS and PL techniques were also employed to analyze the fresh and used

DOI: 10.1021/acsami.6b12278
ACS Appl. Mater. Interfaces 2016, 8, 32887−32900

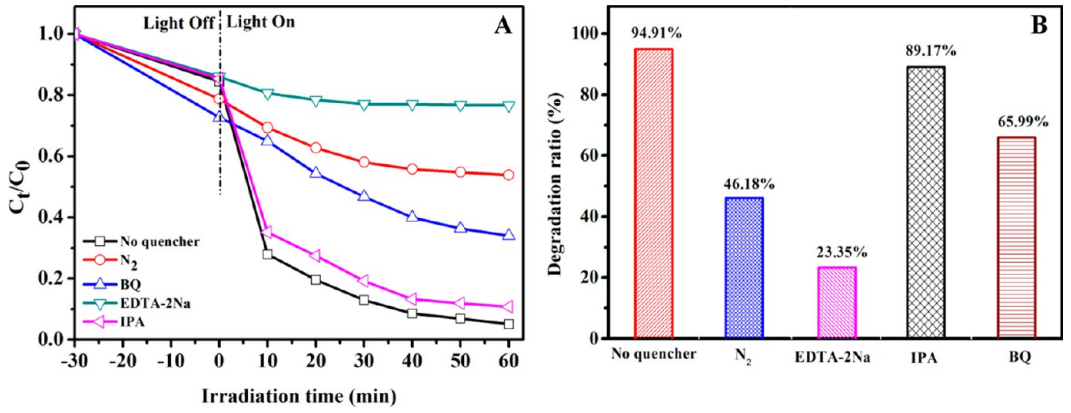

Figure 10. Effect of different quenchers on the photocatalytic oxidation of TC by AgI(20 wt %)/$BiVO_4$ (A, degradation curve; B, corresponding degradation efficiency).

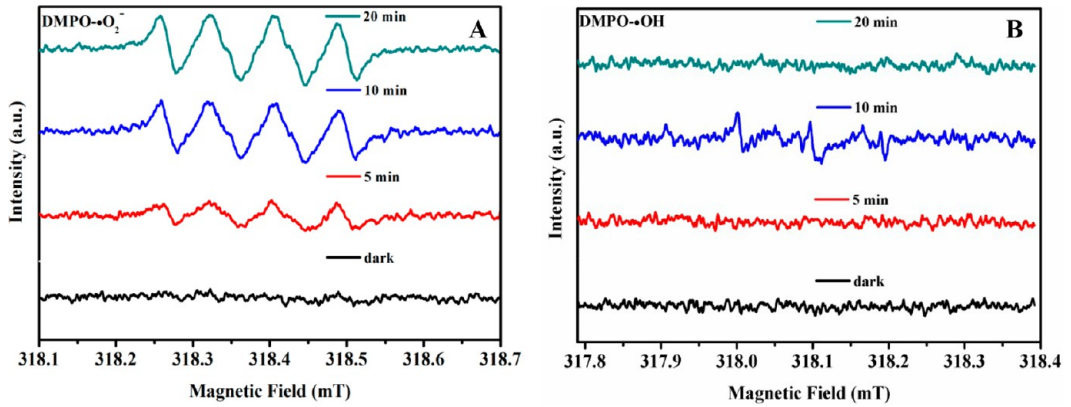

Figure 11. ESR spectra of radical adducts trapped by DMPO spin-trapping in AgI(20 wt %)/$BiVO_4$ dispersion in the dark and under visible light irradiation (irradiation time of 5, 10, and 20 min): (A) in methanol dispersion for DMPO−•O_2^-; and (B) in aqueous dispersion for DMPO−•OH.

sample. The visible light absorption ability of the used catalyst was much better than that of the fresh (Figure 9C), validating that the emergence of metallic Ag was in favor of light absorption. As compared to the fresh sample, the PL intensity of the AgI(20 wt %)/$BiVO_4$ was much lower, indicating that effective charge carriers separation was achieved (Figure 9D). Through the aforementioned characterization methods, the presence of metallic Ag was confirmed, and it could weaken the electron−hole pairs' recombination rate, presented as an improved photocatalytic performance.

3.6. Possible Photodegradation Mechanism. To reveal the dramatic activity enhancement and clarify the intrinsic mechanism of degradation of TC, the roles of main active species were investigated. In this study, three different quenchers, isopropanol (IPA, •OH scavengers), ethylenediaminetetraacetic acid disodium (EDTA-2Na, h^+ scavengers), and 1.4-benzoquinone (BQ, •O_2^- scavengers) were adopted.[28,42] As perceived in Figure 10A,B, the TC decomposition process was significantly inhibited with EDTA-2Na, implying that holes worked in the photocatalytic reaction. Similarly, the addition of BQ also exhibited a negative effect, indicating that •O_2^- radicals had a significant impact in the reaction system. The N_2 purging experiment was further used to confirm the role of •O_2^-, and the degradation efficiencies decreased from 94.91% to 46.18%. In contrast, little efficiency reduction with the addition of IPA demonstrated that •OH might not be the predominant active species. It could deduce that •O_2^- and holes primarily contributed to the photoactivity enhancement, and the action of •OH was the least.

The ESR measurements were performed to confirm the reactive oxygen species evolved in the photocatalysis over AgI(20 wt %)/$BiVO_4$ nanocomposite with 5,5-dimethyl-1-pyrroline *N*-oxide (DMPO) in aqueous solution. As presented in Figure 11A, four obvious signals with AgI(20 wt %)/$BiVO_4$ in methanol were produced, which could be assigned to DMPO−•O_2^- under light illumination, while no •O_2^- signal was observed in the darkness under identical conditions. The obtained ESR information indicated that O_2 in solution was reduced to generate •O_2^- by photogenerated electrons from AgI(20 wt %)/$BiVO_4$ nanocomposite and became the dominant oxygen species during the photocatalytic process. Moreover, no DMPO−•OH signals were detected in aqueous dispersions of AgI(20 wt %)/$BiVO_4$ nanocomposite both in dark condition and under visible light illumination time from 0 to 5 min (Figure 11B). The irradiation time increased to 10 min, and the weak characteristic quadruple peaks of DMPO−•OH adducts were also found, while they disappeared at 20 min. This suggested that fewer •OH radicals generated just participated in the photocatalytic reaction, which was well consistent with a previous report.[42] Thus, the radical trapping experiments and ESR information verified the important role of h^+ and •O_2^-, leading to the enormous photocatalytic activity improvement.

Additionally, the formation of band structure also was important to improve the photoctalytic activity of the

DOI: 10.1021/acsami.6b12278
ACS Appl. Mater. Interfaces 2016, 8, 32887−32900

Scheme 1. Schematic Illustration of the Mechanism for the Photocatalytic Degradation of TC under Visible Light Irradiation over AgI/$BiVO_4$ Nanocomposite: (A) Traditional Model and (B) Z-Scheme Heterojunction System

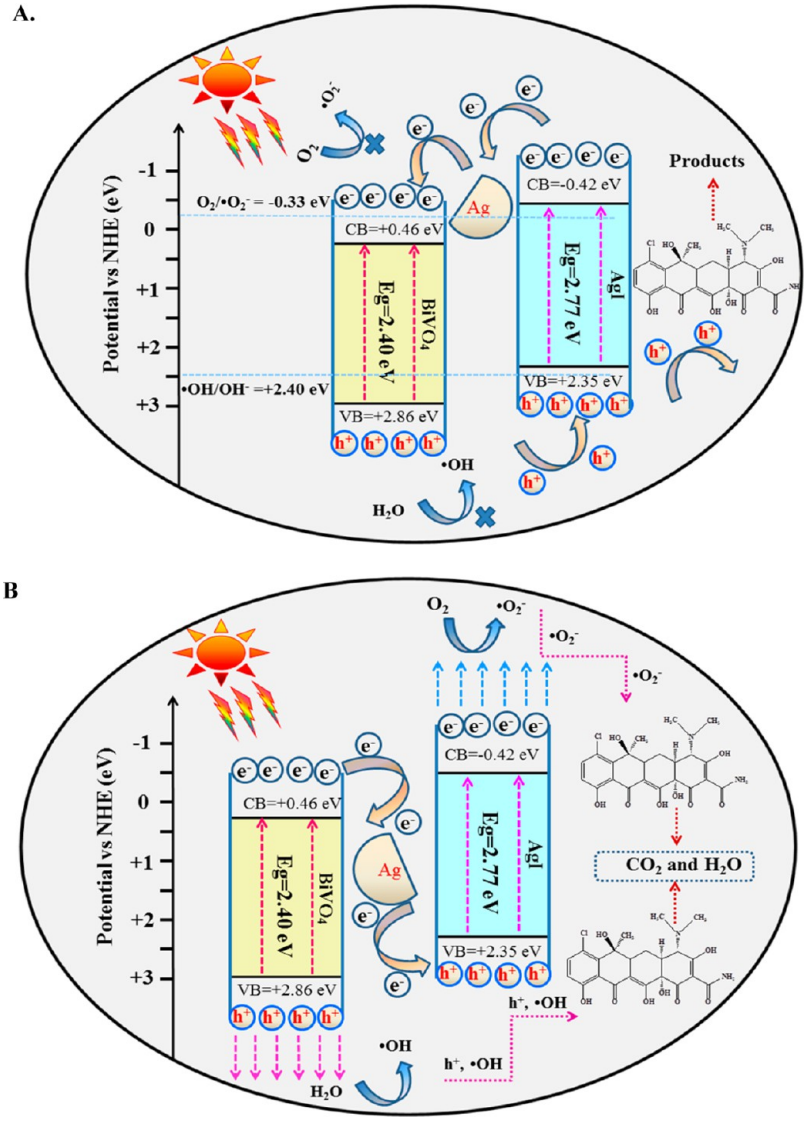

photocatalyst. The conduction band edge (E_{CB}) and value band edge (E_{VB}) of a semiconductor could be acquired by the following formulas (eqs 4 and 5):[21]

$$E_{CB} = X - E^e - 0.5E_g \quad (4)$$

$$E_{VB} = E_{CB} + E_g \quad (5)$$

where X is the absolute electronegativity of the semiconductor, E^e is the energy of free electrons on the hydrogen scale (~4.5 eV), and E_g is the band gap of the semiconductor. The band gap energies of AgI and $BiVO_4$ were perceived to be 2.77 and 2.40 eV in the previous UV−vis DRS discussion. Thus, the E_{VB} of AgI and $BiVO_4$ could be estimated to be +2.35 and +2.86 eV, and the corresponding E_{CB} values were calculated to be −0.42 and +0.46 eV, respectively. As a result, the photogenerated carriers could easily transfer between AgI and $BiVO_4$ because of the band energy potential difference and matching interactive energy band structure.

On the basis of the aforementioned analyses, a reasonable mechanism of TC degradation toward AgI/$BiVO_4$ nanocomposite under visible light is proposed in Scheme 1. It had been verified that the Ag nanoparticles were formed through XRD, XPS, PL, and DRS, and metallic Ag made an important contribution to the photoactivity enhancement. Zhen and his co-workers also found that Ag nanoparticles were generated in Bi_2SiO_5/AgI nanocomposite under visible light irradiation, resulting in superior degradation efficiency for gaseous formaldehyde decomposition.[27] The Ag nanoparticles coated on the AgI surface acted as the charge transmission-bridge to obtain higher charge transfer and electron−hole pairs' separation efficiency in the AgI/Ag/$BiVO_4$ heterojunction. There were two possible photoinduced electrons and holes transferring and separation processes: a traditional model (Scheme 1A) and a Z-scheme heterojunction system (Scheme 1B). As shown in Scheme 1A, photoexcited electrons in the CB of AgI would transfer to that of Ag and were then collected by $BiVO_4$ (eqs 6−9), while the photoinduced holes accumulated on the VB of AgI (eq 10). Although the electron−hole pairs were efficiently separated, the accumulated electrons in the CB of $BiVO_4$ could not reduce O_2 to produce $^{\bullet}O_2^-$, due to the more positive edge potential of $BiVO_4$ (+0.46 eV) than that of $O_2/^{\bullet}O_2^-$ (−0.33 eV vs NHE). Only the transformed holes

DOI: 10.1021/acsami.6b12278
ACS Appl. Mater. Interfaces 2016, 8, 32887−32900

worked in the degradation (eq 11), which did not coincide with the trapping experiments. Thus, the Z-scheme system might be more reasonable. When exposed to visible light illumination, both AgI and $BiVO_4$ were simultaneously excited to generate electrons and holes (eqs 12 and 13). There were two transmission channels for photogenerated electron−hole in the Z-scheme AgI/Ag/$BiVO_4$ system, which could be named as the external and internal transmission channels.[31,32] In the internal part, according to the Z-scheme principal, photoinduced electrons from $BiVO_4$ (CB) could easily flow into metallic Ag through the Schottky barrier (eq 14), which could be attributed to the more negative CB bottom of $BiVO_4$ (+0.46 eV).[44] Because the VB top of AgI (+2.35 eV) was more positive, the obtained photoinduced electrons in Ag could be shifted to the VB top of AgI (eq 15). The transferred electrons on the VB of AgI recombined with the holes there, which was faster than the recombination between e_{CB}^- and h_{VB}^+ of AgI itself (eq 16). Thus, the efficient internal charge transmission could enhance charge carriers' separation efficiency in the AgI/$BiVO_4$ system. With the help of the internal charge transfer, the e_{CB}^- located in the CB of AgI would lead to stronger reduction ability. It suggested that the accumulated electrons in the CB bottom of AgI were transferred to O_2 absorbed on the surface of the heterostructures and promoted $^\bullet O_2^-$ yields because the CB edge potential of AgI was more negative than the standard redox potential E^0 ($O_2/^\bullet O_2^-$) (−0.33 eV vs NHE)[17] (eq 17). The photoinduced holes of $BiVO_4$ directly oxidized TC molecules or H_2O to form $^\bullet$OH radicals $E^0(^\bullet OH/OH^-)$ = +2.40 eV vs NHE.[45] Combined with the above-mentioned results, the role of $^\bullet$OH was verified to be insignificant in the active species trapping experiment, while a slight amount of $^\bullet$OH was also detected in ESR analysis, inferring that the generated $^\bullet$OH only participated in the photocatalytic procedure as the products of the holes (eqs 18 and 19). Not only the predominant active species ($^\bullet O_2^-$ and h^+) but also the converted products ($^\bullet$OH) could effectively degrade TC into CO_2 and H_2O, etc., which finally induce the efficient decomposition of TC (eqs 20 and 22). In conclusion, the Z-scheme charge transfer system significantly enhanced the electrons and holes' transmission and separation, resulting in superior structural stability and enormous enhancement of photocatalytic activity.

(I) Traditional Model:

$$AgI + h\gamma \rightarrow e_{CB}^-(AgI) + h_{VB}^+(AgI) \quad (6)$$

$$BiVO_4 + h\gamma \rightarrow e_{CB}^-(BiVO_4) + h_{VB}^+(BiVO_4) \quad (7)$$

$$e_{CB}^-(AgI) + A_g^* \rightarrow AgI + e_{CB}^-(A_g^*) \quad (8)$$

$$e_{CB}^-(A_g^*) + BiVO_4 \rightarrow A_g^* + e_{CB}^-(BiVO_4) \quad (9)$$

$$h_{VB}^+(BiVO_4) + AgI \rightarrow h_{VB}^+(AgI) + BiVO_4 \quad (10)$$

$$h_{VB}^+(BiVO_4) + TC \rightarrow \text{degradation products } (CO_2 + H_2O) \quad (11)$$

(II) Z-scheme heterojunction system:

$$AgI + h\gamma \rightarrow e_{CB}^-(AgI) + h_{VB}^+(AgI) \quad (12)$$

$$BiVO_4 + h\gamma \rightarrow e_{CB}^-(BiVO_4) + h_{VB}^+(BiVO_4) \quad (13)$$

$$e_{CB}^-(BiVO_4) + A_g^* \rightarrow BiVO_4 + e_{CB}^-(A_g^*) \quad (14)$$

$$e_{CB}^-(A_g^*) \rightarrow \rightarrow \rightarrow h_{VB}^+(AgI) \quad (15)$$

$$e_{CB}^-(A_g^*) + h_{VB}^+(AgI) \rightarrow \text{recombination} \quad (16)$$

$$e_{CB}^-(AgI) + O_2 \rightarrow {}^\bullet O_2^-(AgI) \quad (17)$$

$$h_{VB}^+(BiVO_4) + H_2O \rightarrow {}^\bullet OH(BiVO_4) + H^+ \quad (18)$$

$$OH^- + h_{VB}^+(BiVO_4) \rightarrow {}^\bullet OH(BiVO_4) \quad (19)$$

$$h_{VB}^+(BiVO_4) + TC \rightarrow \text{degradation products } (CO_2 + H_2O)(\text{major}) \quad (20)$$

$$^\bullet O_2^-(AgI) + TC \rightarrow \text{degradation products } (CO_2 + H_2O)(\text{major}) \quad (21)$$

$$^\bullet OH(BiVO_4) + TC \rightarrow \text{degradation products } (CO_2 + H_2O)(\text{slight}) \quad (22)$$

4. CONCLUSIONS

In this study, novel AgI/$BiVO_4$ heterojunctions were successfully synthesized by a facile in situ precipitation approach. The antibiotic tetracycline (TC) was effectively decomposed with the as-prepared catalyst under visible light irradiation, and the degradation process coincided well with the pseudo-first-order kinetic model. The AgI(20 wt %)/$BiVO_4$ nanocomposite exhibited the highest photoactivity, and the degradation efficiency of TC increased approximately 32.23% and 19.48% as compared to bare $BiVO_4$ and AgI, respectively. The emergence of elemental Ag during the photocatalytic reaction would be in favor of constructing AgI/Ag/$BiVO_4$ Z-scheme system. The enhanced visible light absorption, the facilitated photoinduced electrons transfer, and the enhanced separation of photoinduced electron−hole pairs contributed to the improvement of photocatalytic activities. The trapping radicals tests and ESR analysis had demonstrated that $^\bullet O_2^-$ and h^+ were generated in the reaction process. The AgI(20 wt %)/$BiVO_4$ sample also displayed a superior mineralization ability for refractory pollutants, the TOC removal efficiency reached 90.46% within the irradiation time of 120 min, and 3D EEMs analysis also indirectly confirmed the perfect mineralization. This study demonstrates that AgI/$BiVO_4$ could be employed as a promising photocatalyst for water purification using visible light. Constructing Z-scheme heterojunctions might be a good choice to achieve the environmental requirements of VLD photocatalysis for long-term development.

AUTHOR INFORMATION

Corresponding Authors

*E-mail: yangqi@hnu.edu.cn.
*E-mail: dongbowang@hnu.edu.cn.

ORCID

Qi Yang: 0000-0002-9116-6406

Notes

The authors declare no competing financial interest.

DOI: 10.1021/acsami.6b12278
ACS Appl. Mater. Interfaces 2016, 8, 32887−32900

■ ACKNOWLEDGMENTS

We sincerely thank the National Natural Science Foundation of China (NSFC) (nos. 51378188, 51478170, and 51508178) for financial support.

■ REFERENCES

(1) Asahi, R.; Morikawa, T.; Ohwaki, T.; Aoki, K.; Taga, Y. Visible-Light Photocatalysis in Nitrogen-Doped Titanium Oxides. *Science* **2001**, *293*, 269−271.

(2) Baransi, K.; Dubowski, Y.; Sabbah, I. Synergetic Effect between Photocatalytic Degradation and Adsorption Processes on the Removal of Phenolic Compounds from Olive Mill Wastewater. *Water Res.* **2012**, *46*, 789−798.

(3) Lin, X.; Guo, X. Y.; Shi, W. L.; Guo, F.; Che, G. B.; Zhai, H. J.; Yan, Y. S.; Wang, Q. W. Ag_3PO_4 Quantum Dots Loaded on the Surface of Leaf-like $InVO_4/BiVO_4$ Heterojunction with Enhanced Photocatalytic Activity. *Catal. Commun.* **2015**, *71*, 21−27.

(4) Lin, X.; Yu, S. Y.; Gao, Z. Y.; Zhang, X. X.; Che, G. B. Heterostructured RGO/$Bi_{3.64}Mo_{0.36}O_{6.55}$ Nanospheres: Synthesis and Enhanced Visible-Light-Driven Photocatalytic Activity. *J. Mol. Catal. A: Chem.* **2016**, *411*, 40−47.

(5) Hong, Y. Z.; Jiang, Y. H.; Li, C. S.; Fan, W. Q.; Yan, X.; Yan, M.; Shi, W. D. In-situ Synthesis of Direct Solid-state Z-scheme V_2O_5/g-C_3N_4 Heterojunctions with Enhanced Visible Light Efficiency in Photocatalytic Degradation of Pollutants. *Appl. Catal., B* **2016**, *180*, 663−673.

(6) Chen, F.; Yang, Q.; Li, X. M.; Zeng, G. M. Hierarchical Assembly of Graphene-bridged Ag_3PO_4/Ag/$BiVO_4$(040) Z-scheme Photocatalyst: An Efficient, Sustainable and Heterogeneous Catalyst with Enhanced Visible-light Photoactivity towards Tetracycline Degradation under Visible Light Irradiation. *Appl. Catal., B* **2017**, *200*, 330−342.

(7) Kudo, A.; Miseki, Y. Heterogeneous Photocatalyst Materials for Water Splitting. *Chem. Soc. Rev.* **2009**, *38* (1), 253−278.

(8) Lin, X.; Guo, X. Y.; Shi, W. L.; Zhao, L. N.; Yan, Y. S.; Wang, Q. W. Ternary Heterostructured Ag-$BiVO_4/InVO_4$ Composites: Synthesis and Enhanced Visible-Light-Driven Photocatalytic Activity. *J. Alloys Compd.* **2015**, *635*, 256−264.

(9) Khan, S. U.; Al-Shahry, M.; Ingler, W. B. Efficient Photochemical Water Splitting by a Chemically Modified n-TiO_2. *Science* **2002**, *297*, 2243−2245.

(10) Xiong, T.; Wen, M. Q.; Dong, F.; Yu, J. Y. Three Dimensional Z-scheme $(BiO)_2CO_3/MoS_2$ with Enhanced Visible Light Photocatalytic NO Removal. *Appl. Catal., B* **2016**, *199*, 87−95.

(11) Chen, F.; Yang, Q.; Niu, C. G.; Li, X. M.; Zhang, C.; Zeng, G. M. Plasmonic Photocatalyst Ag@AgCl/$ZnSn(OH)_6$: Synthesis, Characterization and Enhanced Visible Light Photocatalytic Activity in the Decomposition of Dyes and Phenol. *RSC Adv.* **2015**, *5*, 63152−63164.

(12) Joo, J. B.; Dahl, M.; Li, N.; Zaera, F.; Yin, Y. Tailored Synthesis of Mesoporous TiO_2 Hollow Nanostructures for Catalytic Applications. *Energy Environ. Sci.* **2013**, *6*, 2082−2092.

(13) Park, Y.; McDonald, K. J.; Choi, K. S. Progress in Bismuth Vanadate Photoanodes for Use in Solar Water Oxidation. *Chem. Soc. Rev.* **2013**, *42*, 2321−2337.

(14) Hong, S. J.; Lee, S.; Jang, J. S.; Lee, J. S. Heterojunction $BiVO_4$/WO_3 Electrodes for Enhanced Photoactivity of Water Oxidation. *Energy Environ. Sci.* **2011**, *4*, 1781−1787.

(15) Chen, F.; Yang, Q.; Zhong, Y.; An, H. X.; Zhao, J. W.; Xie, T. Photo-reduction of Bromate in Drinking Water by Metallic Ag and Reduced Graphene Oxide (RGO) Jointly Modified $BiVO_4$ under Visible Light Irradiation. *Water Res.* **2016**, *101*, 555−563.

(16) Yan, X.; Wang, X. Y.; Gu, W.; Wu, M. M. Single-crystalline $AgIn(MoO_4)_2$ Nanosheets Grafted Ag/AgBr Composites with Enhanced Plasmonic Photocatalytic Activity for Degradation of Tetracycline under Visible Light. *Appl. Catal., B* **2015**, *164*, 297−304.

(17) Xu, Y. S.; Zhang, W. D. Anion Exchange Strategy for Construction of Sesame-biscuit-like $Bi_2O_2CO_3/Bi_2MoO_6$ Nanocomposites with Enhanced Photocatalytic Activity. *Appl. Catal., B* **2013**, *140−141*, 306−316.

(18) Mu, J. B.; Chen, B.; Zhang, M. Y.; Guo, Z. C.; Zhang, P.; Zhang, Z. Y. Enhancement of the Visible-light Photocatalytic Activity of In_2O_3-TiO_2 Nanofiber Heteroarchitectures. *ACS Appl. Mater. Interfaces* **2012**, *4*, 424−430.

(19) Yan, M.; Wu, Y. L.; Yan, Y.; Yan, X.; Zhu, F. F.; Hua, Y. Q.; Shi, W. D. Synthesis and Characterization of Novel $BiVO_4/Ag_3VO_4$ Heterojunction with Enhanced Visible-Light-Driven Photocatalytic Degradation of Dyes. *ACS Sustainable Chem. Eng.* **2016**, *4*, 757−766.

(20) Zhao, W.; Liu, Y.; Wei, Z. B.; Yang, S. G.; He, H.; Sun, C. Fabrication of a Novel p-n Heterojunction Photocatalyst n-$BiVO_4$@p-MoS_2 with Core-shell Structure and Its Excellent Visible-light Photocatalytic Reduction and Oxidation Activities. *Appl. Catal., B* **2016**, *185*, 242−252.

(21) Yuan, Q.; Chen, L.; Xiong, M.; He, J.; Luo, S. L.; Au, C. T.; Yin, S. F. $Cu_2O/BiVO_4$ Heterostructures: Synthesis and Application in Simultaneous Photocatalytic Oxidation of Organic Dyes and Reduction of Cr(VI) under Visible Light. *Chem. Eng. J.* **2014**, *255*, 394−402.

(22) Gao, X. H.; Wu, H. B.; Zheng, L. X.; Zhong, Y. J.; Hu, Y. Formation of Mesoporous Heterostructured $BiVO_4/Bi_2S_3$ Hollow Discoids with Enhanced Photoactivity. *Angew. Chem., Int. Ed.* **2014**, *53*, 5917−5921.

(23) Huang, H. W.; He, Y.; Du, X.; Chu, P. K.; Zhang, Y. H. A General and Facile Approach to Heterostructured Core/Shell $BiVO_4$/BiOI p-n Junction: Room-Temperature in Situ Assembly and Highly Boosted Visible-Light Photocatalysis. *ACS Sustainable Chem. Eng.* **2015**, *3* (12), 3262−3273.

(24) Yu, H. G.; Xu, L. L.; Wang, P.; Wang, X. F.; Yu, J. G. Enhanced Photoinduced Stability and Photocatalytic Activity of AgBr Photocatalyst by Surface Modification of Fe(III) Cocatalyst. *Appl. Catal., B* **2014**, *144*, 75−82.

(25) Zhang, H.; Fan, X. F.; Quan, X.; Chen, S.; Yu, H. T. Graphene Sheets Grafted Ag@AgCl Hybrid with Enhanced Plasmonic Photocatalytic Activity under Visible Light. *Environ. Sci. Technol.* **2011**, *45*, 5731−5736.

(26) Yan, J.; Wang, C.; Xu, H.; Xu, Y. G.; She, X. J.; Chen, J. J. AgI/Ag_3PO_4 Heterojunction Composites with Enhanced Photocatalytic Activity under Visible Light Irradiation. *Appl. Surf. Sci.* **2013**, *287*, 178−186.

(27) Wan, Z.; Zhang, G. K. Synthesis and Facet-dependent Enhanced Photocatalytic Activity of Bi_2SiO_5/AgI Nanoplate Photocatalysts. *J. Mater. Chem. A* **2015**, *3*, 16737−16745.

(28) Chen, F.; Yang, Q.; Niu, C. G.; Li, X. M.; Zhang, C.; Zhao, J. W. Enhanced Visible Light Photocatalytic Activity and Mechanism of $ZnSn(OH)_6$ Nanocubes Modified with AgI Nanoparticles. *Catal. Commun.* **2016**, *73*, 1−6.

(29) Wang, Q.; Shi, X. D.; Xu, J. J.; Crittenden, J. C.; Liu, E. Q.; Zhang, Y.; Cong, Y. Q. Highly Enhanced Photocatalytic Reduction of Cr(VI) on AgI/TiO_2 under Visible Light Irradiation: Influence of Calcination Temperature. *J. Hazard. Mater.* **2016**, *307*, 213−220.

(30) Ye, H. F.; Lin, H. L.; Cao, J.; Chen, S. F.; Chen, Y. Enhanced Visible Light Photocatalytic Activity and Mechanism of $BiPO_4$ Nanorods Modified with AgI Nanoparticles. *J. Mol. Catal. A: Chem.* **2015**, *397*, 85−92.

(31) Chen, Z. H.; Wang, W. L.; Zhang, Z. G.; Fang, X. L. High-efficiency Visible-light-driven Ag_3PO_4/AgI Photocatalysts: ZScheme Photocatalytic Mechanism for Their Enhanced Photocatalytic Activity. *J. Phys. Chem. C* **2013**, *117*, 19346−19352.

(32) Ye, L. Q.; Liu, J. Y.; Gong, C. Q.; Tian, L. H.; Peng, T. Y.; Zan, L. Two Different Roles of Metallic Ag on Ag/AgX/BiOX (X = Cl, Br) Visible Light Photocatalysts: Surface Plasmon Resonance and Z-scheme Bridge. *ACS Catal.* **2012**, *2*, 1677−1683.

(33) Wang, X. F.; Li, S. F.; Ma, Y. Q.; Yu, H. G.; Yu, J. G. $H_2WO_4 \cdot 3H_2O$/Ag/AgCl Composite Nanoplates: A Plasmonic Z-scheme Visible Light Photocatalyst. *J. Phys. Chem. C* **2011**, *115*, 14648−14655.

DOI: 10.1021/acsami.6b12278
ACS Appl. Mater. Interfaces 2016, 8, 32887−32900

(34) He, Y. M.; Zhang, L. H.; Teng, B. T.; Fan, M. H. New Application of ZScheme Ag_3PO_4/gC_3N_4 Composite in Converting CO_2 to Fuel. *Environ. Sci. Technol.* **2015**, *49*, 649−656.
(35) Li, C. J.; Zhang, P.; Lv, R.; Lu, J. W.; Wang, T.; Wang, S. P.; Wang, H. F.; Gong, J. L. Selective Deposition of Ag_3PO_4 on Monoclinic $BiVO_4$ (040) for Highly Efficient Photocatalysis. *Small* **2013**, *9* (23), 3951−3956.
(36) Cheng, H. F.; Wang, W. J.; Huang, B. B.; Wang, Z. Y.; Zhan, J.; Qin, X. Y. Tailoring AgI Nanoparticles for the Assembly of AgI/BiOI Hierarchical Hybrids with Size-dependent Photocatalytic Activities. *J. Mater. Chem. A* **2013**, *1*, 7131−7136.
(37) He, Z. Q.; Shi, Y. Q.; Gao, C.; Wen, L. N.; Chen, J. M.; Song, S. $BiOCl/BiVO_4$ p-n Heterojunction with Enhanced Photocatalytic Activity under Visible-light Irradiation. *J. Phys. Chem. C* **2014**, *118*, 389−398.
(38) Li, H. Y.; Sun, Y. J.; Cai, B.; Gan, S. Y.; Han, D. X.; Niu, L.; Wu, T. S. Hierarchically Z-scheme Photocatalyst of Ag@AgCl Decorated on $BiVO_4$ (040) with Enhancing Photoelectrochemical and Photocatalytic Performance. *Appl. Catal., B* **2015**, *170−171*, 206−214.
(39) Wang, H.; Yuan, X. Z.; Wu, Y.; Zeng, G. M.; Dong, H. R.; Chen, X. H.; Leng, L. J. In Situ Synthesis of In_2S_3@MIL-125(Ti) Core-shell Microparticle for the Removal of Tetracycline from Wastewater by Integrated Adsorption and Visible-Light-Driven Photocatalysis. *Appl. Catal., B* **2016**, *186*, 19−29.
(40) Shi, Y.; Xing, S.; Wang, X.; Wang, S. Changes of the Reactor Performance and the Properties of Granular Sludge under Tetracycline Stress. *Bioresour. Technol.* **2013**, *139*, 170−175.
(41) Song, C.; Sun, X. F.; Xing, S. F.; Xia, P. F.; Shi, Y. J.; Wang, S. G. Characterization of the Interactions between Tetracycline Antibiotics and Microbial Extracellular Polymeric Substances with Spectroscopic Approaches. *Environ. Sci. Pollut. Res.* **2014**, *21*, 1786−1795.
(42) Zhang, Z. Y.; Jiang, D. L.; Li, D.; He, M. Q.; Chen, M. Construction of $SnNb_2O_6$ Nanosheet/g-C_3N_4 Nanosheet Two-dimensional Heterostructures with Improved Photocatalytic Activity: Synergistic Effect and Mechanism Insight. *Appl. Catal., B* **2016**, *183*, 113−123.
(43) Huang, Y. C.; Fan, W. J.; Long, B.; Li, H. B.; Zhao, F. Y.; Liu, Z. L.; Tong, Y. X. Visible light $Bi_2S_3/Bi_2O_3/Bi_2O_2CO_3$ Photocatalyst for Effective Degradation of Organic Pollutions. *Appl. Catal., B* **2016**, *185*, 68−76.
(44) Wang, Y.; Niu, C. N.; Zhang, L.; Wang, Y.; Zhang, H.; Huang, D. W. High-efficiency Visible-light $AgI/Ag/Bi_2MoO_6$ as a Z-scheme Photocatalyst for Environmental Applications. *RSC Adv.* **2016**, *6* (13), 10221−10228.
(45) Xia, J. X.; Di, J.; Li, H. T.; Xu, H.; Li, H. M.; Guo, S. J. Ionic Liquid-induced Strategy for Carbon Quantum Dots/BiOX (X= Br, Cl) Hybrid Nanosheets with Superior Visible-Light-Driven Photocatalysis. *Appl. Catal., B* **2016**, *181*, 260−269.

DOI: 10.1021/acsami.6b12278
ACS Appl. Mater. Interfaces 2016, 8, 32887−32900